

Disassembly Mechanisms and Energetics of Polymetallic Rings and Rotaxanes

Niklas Geue, Tom S. Bennett, Alexandra-Ana-Maria Arama, Lennart A. I. Ramakers, George F. S. Whitehead, Grigore A. Timco, P. B. Armentrout, Eric J. L. McInnes, Neil A. Burton, Richard E. P. Winpenney, and Perdita E. Barran*



Cite This: *J. Am. Chem. Soc.* 2022, 144, 22528–22539



Read Online

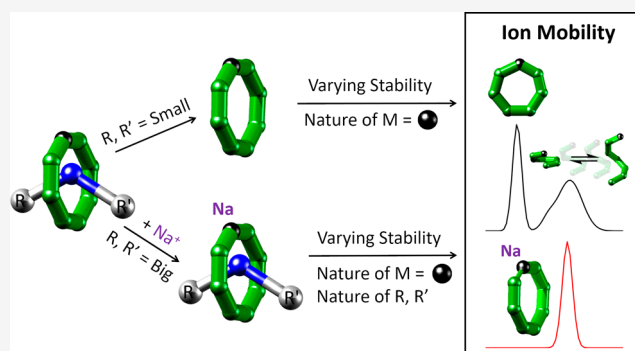
ACCESS |

Metrics & More

Article Recommendations

Supporting Information

ABSTRACT: Understanding the fundamental reactivity of polymetallic complexes is challenging due to the complexity of their structures with many possible bond breaking and forming processes. Here, we apply ion mobility mass spectrometry coupled with density functional theory to investigate the disassembly mechanisms and energetics of a family of heterometallic rings and rotaxanes with the general formula $[\text{NH}_2\text{RR}'][\text{Cr}_7\text{MF}_8(\text{O}_2\text{C}^t\text{Bu})_{16}]$ with $\text{M} = \text{Mn}^{\text{II}}, \text{Fe}^{\text{II}}, \text{Co}^{\text{II}}, \text{Ni}^{\text{II}}, \text{Cu}^{\text{II}}, \text{Zn}^{\text{II}}, \text{Cd}^{\text{II}}$. Our results show that their stability can be tuned both by altering the d-metal composition in the macrocycle and by the end groups of the secondary ammonium cation $[\text{NH}_2\text{RR}]^+$. Ion mobility probes the conformational landscape of the disassembly process from intact complex to structurally distinct isobaric fragments, providing unique insights to how a given divalent metal tunes the structural dynamics.



INTRODUCTION

Ion mobility mass spectrometry (IM-MS) allows both the mass and structure of isolated ions to be measured in the same experiment.^{1–4} Ion mobility measurements for any given analyte can be converted to the structural parameter collision cross sections (CCS), which can be compared to those predicted from theoretical candidate geometries. IM-MS has been widely applied to examine the dynamics of the disassembly of protein complexes^{5–8} but far less often to determine the relationship between conformation and stability of synthetic macromolecular complexes. A number of studies have demonstrated the use of IM-MS for the characterization of polymetallic compounds,^{9–15} but only a handful have used it to explore disassembly processes. For example, Wesdemiotis and co-workers showed the collisional activation of a terpyridine-based hexameric Cd-complex and subsequently used ion mobility to separate the macrocyclic precursor ion from linear isomers.¹⁶ In another study, Mallis *et al.* investigated pyridine-based Pt-rhomboids and demonstrated, among other things, different gas phase stabilities of isobaric complexes with activated IM-MS.¹⁷ More recently, Baksi *et al.* used IM-MS to visualize the energetically driven reaction between coin metal thiolate clusters, in which silver atoms were incrementally exchanged for gold centers.¹⁸ Although these are interesting examples, a systematic application of IM-MS to investigate the reactivity or disassembly of polymetallic

complexes as a function of structure and metals present has not yet been reported.

We hypothesized that IM-MS would be an ideal method to investigate these systems and that it could be used to rationalize the stability of isostructural complexes as a function of the metal present along with conformation-specific information. An attractive chemical problem to answer with this approach is the conformational rigidity of rotaxanes with respect to their threads (herein used as a synonym for “axles”). To address these challenges, we use IM-MS supported by density functional theory (DFT) to characterize the heterometallic rings $[\text{Cr}_7\text{MF}_8(\text{O}_2\text{C}^t\text{Bu})_{16}]^-$ (“ Ring_M^- ”, $\text{M} = \text{Mn}^{\text{II}}, \text{Fe}^{\text{II}}, \text{Co}^{\text{II}}, \text{Ni}^{\text{II}}, \text{Cu}^{\text{II}}, \text{Zn}^{\text{II}}, \text{Cd}^{\text{II}}$) alone as well as in hybrid organic–inorganic [2]-rotaxane families of the formula $[\text{NH}_2\text{RR}'][\text{Ring}_M^-]$ (“ Ph_M ” and “ Am_M ”), where R and R’ are terminated by bulky phenyl or *tert*-butyl groups such that the secondary ammonium cation threads through $[\text{Ring}_M^-]$ (Ph_M : thread “ TPh^+ ” (“Phenyl”) = $[\text{NH}_2(\text{CH}_2\text{C}_6\text{H}_5)-(\text{CH}_2\text{CH}_2\text{C}_6\text{H}_5)]^+$; Am_M : thread “ TAm^+ ” (“Amide”) =

Received: July 30, 2022

Published: December 2, 2022

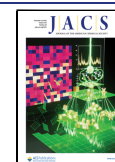
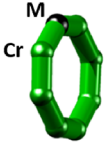
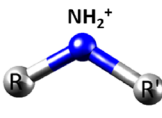
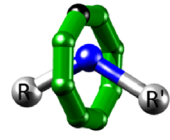
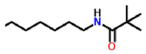
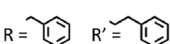
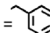
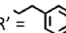


Table 1. Overview of the Studied Polymetallic Systems (Rings, Threads, and Rotaxanes), Including their Chemical Formulas and the Substituents to the Building Blocks

	Ring	Thread	Rotaxane
Cartoon of the Studied Molecular Building Blocks			
Nomenclature	$[\text{Ring}_M]^-$ = $[\text{Cr}_7\text{MF}_8\text{Piv}_{16}]^-$	TAm^+ and TPh^+ = $[\text{NH}_2\text{RR}']^+$	Am_M and Ph_M = $[\text{NH}_2\text{RR}'][\text{Cr}_7\text{MF}_8\text{Piv}_{16}]^-$
Substituents to the Building Blocks	M = Mn ^{II} , Fe ^{II} , Co ^{II} , Ni ^{II} , Cu ^{II} , Zn ^{II} , Cd ^{II}	TAm^+ : R = R' =  TPh^+ :  R =  R' = 	M = Mn ^{II} , Fe ^{II} , Co ^{II} , Ni ^{II} , Cu ^{II} , Zn ^{II} , Cd ^{II} $[\text{NH}_2\text{RR}'] = \text{TAm}^+, \text{TPh}^+$

$[\text{NH}_2(\text{C}_6\text{H}_{12}\text{NHC}(\text{O})^t\text{Bu})_2]^+$. The studied compounds and their building blocks are illustrated in Table 1.

In our analysis, we consider if the Irving–Williams series and other arguments, often developed for monometallic complexes and rationalized by crystal field theory, are transferable to polymetallic complexes. We show that IM-MS can qualitatively and quantitatively investigate the disassembly, conformational dynamics, and stabilities of these compounds. The specific systems studied have been proposed as qubits for quantum information processing,¹⁹ and the ability to link the rings into multiple qubit arrays²⁰ is a key advantage that this approach has over more conventional approaches. Understanding the stability of the compounds is important in order to make increasingly complex molecules for specific quantum applications, e.g., synthesis of a five-spin supramolecule that could be used to simulate decoherence in Bell states.²¹ As supramolecular chemistry using polymetallic units as building blocks develops,^{22–25} the understanding of ligand metathesis achieved here should be important in designing future synthesis routes.

RESULTS

Heterometallic Rings $[\text{Cr}_7\text{MF}_8(\text{O}_2\text{C}^t\text{Bu})_{16}]^- = [\text{Ring}_M]^-$. The heterometallic rings $[\text{Ring}_M]^-$ studied consist of seven chromium(III) ions and one divalent metal center, arranged in a regular octagon with each edge bridged by one fluoride inside the ring and two pivalate ligands ($\text{O}_2\text{C}^t\text{Bu} = \text{Piv}$) outside the ring (Figure 1a, inset for M = Mn^{II}).²⁶ On each edge, there is one axial and one equatorial pivalate, with respect to the Cr_7M plane, with the axial position alternating “up” and “down” around the ring. Following optimization of the ionization source and solvent conditions, mass spectra of $[\text{NH}_2\text{RR}']^+[\text{Ring}_M]^-$ (R = R' = CH₃ for M = Mn^{II}, Co^{II}, Ni^{II}, Cu^{II}, Zn^{II}, Cd^{II} and R = R' = C₂H₅ for M = Fe^{II}) were recorded in positive and negative modes. For all species, intact rings were observed as anions (Figure S1a for M = Mn^{II}, Supplementary Data Set for other M). The assignments of all $[\text{Ring}_M]^-$ species, and all other ions discussed in this study, were informed by accurate masses and isotopic distributions, which were typically in high accordance with prediction (Figure S1b for $[\text{Ring}_{\text{Mn}}]^-$).

Disassembly and Stability Trend of $[\text{Ring}_M]^-$. To understand how altering the d-metal composition affects the ring energetics, we isolated each ring and ramped the energy at which it is activated by collisions while recording the arrival

time distribution (ATD) of the precursor and product ions. We extracted the CCS as a function of the collision energy for all ions. In the tandem mass spectra (MS^2), common product ions were observed, indicating similar fragmentation pathways. For example, the precursor ion $[\text{Ring}_{\text{Mn}}]^-$ at $m/z = 2188$ follows dissociation channels that all involve the loss of a metal center along with ligands (Figure 1a), suggesting substantial perturbation of the ring geometry. We identified the products and reaction pathways including the loss of the manganese and two pivalate ligands (reaction to $[\text{Cr}_7\text{F}_8\text{Piv}_{14}]^- = \mathbf{1}$), the loss of one chromium center, two pivalates and one fluoride (reaction to $[\text{Cr}_6\text{MnF}_7\text{Piv}_{14}]^- = \mathbf{2}$), or one chromium and three pivalate ligands (reaction to $[\text{Cr}_6\text{MnF}_8\text{Piv}_{13}]^- = \mathbf{3}$, Figure 1a). Ion mobility allows us to consider the conformations of the precursor and product ions. While $[\text{Ring}_{\text{Mn}}]^-$ presents a discrete unimodal conformer centered at $\text{CCS}_{\text{N}_2} = 438 \text{ \AA}^2$ at this collision energy, remarkably for all fragmentation channels, the product ions are structurally diverse, with narrow, unimodal conformers at lower CCS_{N_2} (compact, “C”) as well as wide, multimodal distributions with higher CCS_{N_2} (extended, “E”, Figure 1b). The nature of these disassembled products is investigated further below.

For all $[\text{Ring}_M]^-$ (M = Mn^{II}, Fe^{II}, Co^{II}, Ni^{II}, Cu^{II}, Zn^{II}, Cd^{II}), the fragmentation behavior is similar and results in **1** as the main product. This preference for **1** over the structures similar to **2** and **3** (different M) is more pronounced for Ni^{II}, Zn^{II}, Cd^{II}, and particularly Cu^{II} (Supplementary Data Set). The energy needed to break the $[\text{Ring}_M]^-$ structure, predominantly yielding **1**, also varies (Figure 1c) and was quantified with E_{50} values (Table S1, Figure 1d) obtained from the corresponding survival yield plots (Figure 1c). The results show that $[\text{Ring}_{\text{Ni}}]^-$ is the most stable ion and exhibits a 22% higher E_{50} value than the least stable species $[\text{Ring}_{\text{Cu}}]^-$.

Combining Ion Mobility and DFT for $[\text{Ring}_M]^-$ and Their Fragments. The CCS_{N_2} values for each $[\text{Ring}_M]^-$ were similar, with $[\text{Ring}_{\text{Cd}}]^-$ and $[\text{Ring}_{\text{Mn}}]^-$ being slightly larger than the other species (Table S2). DFT optimized structures were generated for all $[\text{Ring}_M]^-$ (Figure S2 for M = Mn^{II}), from which we obtained CCS_{N_2} values using the trajectory method of IMoS.²⁷ These were found to be ~8% larger than experiment (Table S2). To investigate this slight discrepancy, two hypothetical ring conformers (Figures S3 and S4) and two open isomers (Figures S5–S7) were generated for $[\text{Ring}_{\text{Mn}}]^-$

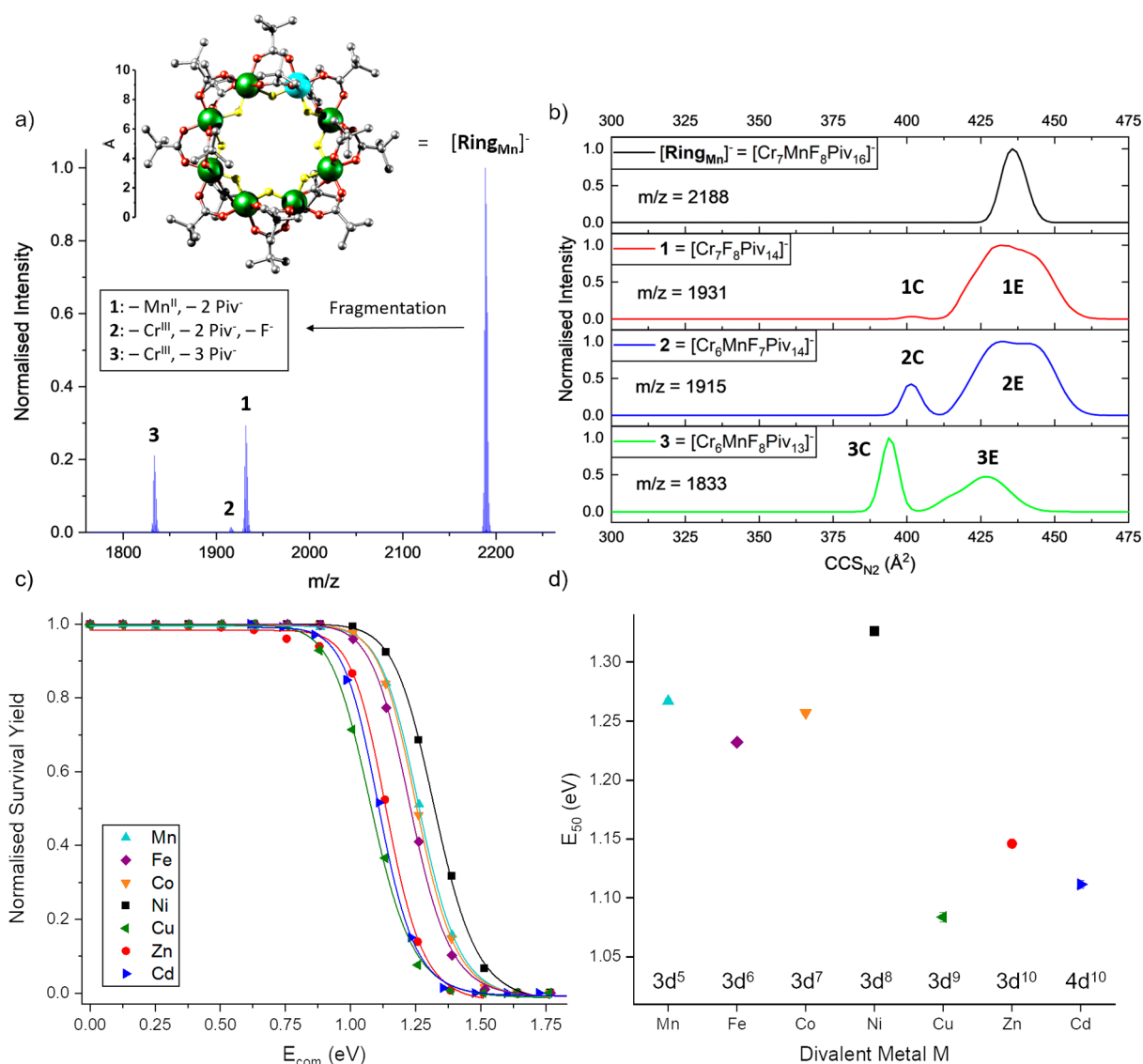


Figure 1. (a) MS² data from $[\text{NH}_2(\text{CH}_3)_2][\text{Ring}_{\text{Mn}}]^-$ (10 μM in 500 μM NaI and 4:1 toluene/methanol) at $E_{\text{lab}} = 110$ eV, following selection of $[\text{Ring}_{\text{Mn}}]^-$ ($m/z = 2188$). Inset: structure of $[\text{Ring}_{\text{Mn}}]^-$ (Cr: green, Mn: cyan, F: yellow, O: red, C: gray) with an Å ruler based on crystal structure coordinates. Hydrogen atoms in the *tert*-butyl groups were omitted for clarity. (b) CCS_{N₂} Distributions of $[\text{Ring}_{\text{Mn}}]^-$ and selected fragments (1–3) at $E_{\text{lab}} = 110$ eV. (c) Normalized survival yield vs E_{com} for $[\text{Ring}_{\text{Mn}}]^-$ fitted to a sigmoidal Hill function ($M = \text{Mn}$: cyan, Fe: purple, Co: orange, Ni: black, Cu: green, Zn: red, Cd: blue). (d) E_{50} values for the dissociation of the anionic rings $[\text{Ring}_{\text{M}}]^-$ with respect to M (Table S1). Error bars are shown and in most cases are smaller than the symbol size.

and their theoretical CCS_{N₂} values enumerated (Table S3). The two conformers yield slightly smaller but similar values to that of the DFT optimized $[\text{Ring}_{\text{Mn}}]^-$ structure, whereas the open isomers gave even higher values. Therefore, the candidate structures unlikely account for the observed differences between the experimental and predicted CCS_{N₂} values of $[\text{Ring}_{\text{M}}]^-$. We attribute this systematic difference to the lack of refinement of the trajectory method for metallosupramolecular systems (Figures S8 and S9).

As discussed above, changes in arrival time distribution of $[\text{Ring}_{\text{Mn}}]^-$ were recorded as a function of incremental increases in collision energy, showing the onset of ring dissociation and the corresponding appearance of fragment ions (Figure S10). Although there is little evidence of any substantial change in the conformation of the ring prior to dissociation, at low energies, $[\text{Ring}_{\text{Mn}}]^-$ contracts slightly before expanding again. The product ions present distinct

conformational families C and E (Figure 1b). The relative population of these distributions differ significantly between the fragments but also with respect to the divalent metal M as observed from measurements on other $[\text{Ring}_{\text{M}}]^-$ precursors (Supplementary Data Set). Surprisingly, the relative populations of C and E in the homometallic Cr₇-fragment 1 allow us to distinguish which divalent metal M was present in the precursor $[\text{Ring}_{\text{M}}]^-$. Significant amounts of 1C are observed for Cu^{II}, Zn^{II}, and Cd^{II} (Figure S11 for $M = \text{Cu}^{\text{II}}$), whereas almost no 1C is seen for Mn^{II}, Fe^{II}, Co^{II}, and Ni^{II} (Figures S12 and S13 for $M = \text{Mn}^{\text{II}}$, Ni^{II}). For the less dominant product ions 2 and 3, the observed differences between M are more subtle.

To rationalize this behavior, additional experiments and calculations were carried out for fragment 3 with $M = \text{Mn}^{\text{II}}$. Each distribution was selected, reinserted in the drift ring, and again, ion mobility separated in one to three passes (IMS²).

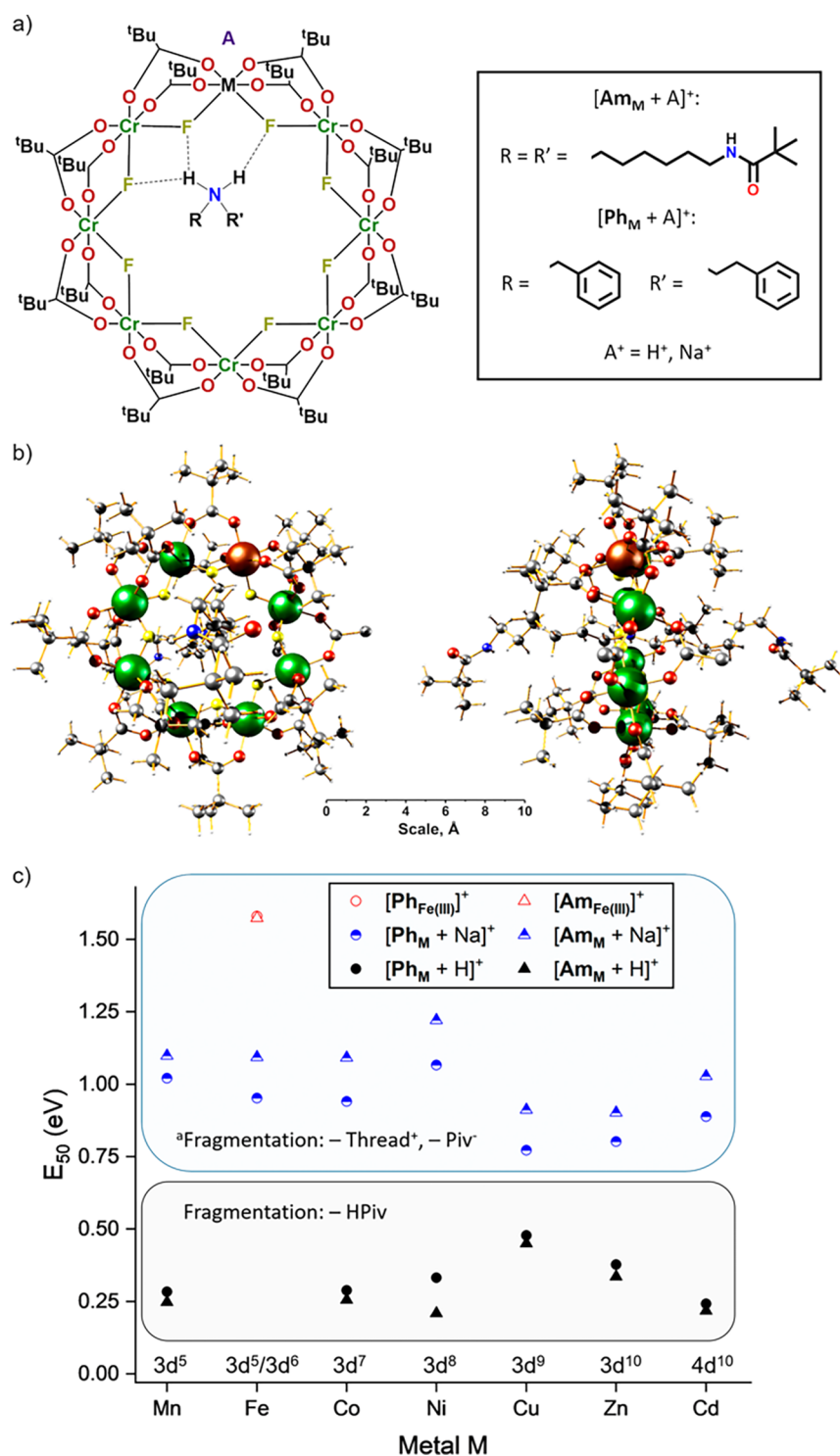


Figure 2. (a) Schematic of $[\text{Am}_M + \text{A}]^+$ and $[\text{Ph}_M + \text{A}]^+$. The thread is found at the ring center with the two protons on the ammonium nitrogen exhibiting hydrogen bonds to the fluorides. Hydrogen bonding, shown in the figure (dashed lines), partially localizes the divalent metal site due to the greater electron density on the fluorides bound to M^{II} . The location of the charge carrier A^+ likely depends on both A^+ and the thread, which is further discussed in another report.²⁸ (b) Single crystal X-ray structure of Am_{Ni} ²⁹ in front (left) and side views (right) including dimensions in Å (Ni: brown, Cr: dark green, F: yellow, O: red, N: blue, C: gray, H: white). Solvent molecules in the asymmetric unit have been removed for clarity. The Ni sites in the $[\text{Ring}_{\text{Ni}}]^-$ unit are disordered over multiple positions. (c) E_{50} values for the fragmentation of the rotaxane cations $[\text{Ph}_M + \text{A}]^+$ and $[\text{Am}_M + \text{A}]^+$ ($\text{A}^+ = \text{H}^+, \text{Na}^+$) with respect to M , as well as the E_{50} values of the oxidized Fe^{III} species $[\text{Ph}_{\text{Fe}(\text{III})}]^+$ and $[\text{Am}_{\text{Fe}(\text{III})}]^+$. An overlap in the mass spectra with these species prevented further investigation of the protonated ions $[\text{Ph}_{\text{Fe}} + \text{H}]^+$ and $[\text{Am}_{\text{Fe}} + \text{H}]^+$.^f For the ion $[\text{Am}_{\text{Cu}} + \text{Na}]^+$, the main fragmentation channel is $-\text{Cu}^{\text{II}}, -2 \text{Piv}^-$ (Figure S29). Error bars are omitted for clarity but in all cases are smaller than the symbol size (Table S1). The electron configuration of Fe depends on the oxidation state ($\text{Fe}^{\text{II}}: 3d^6, \text{Fe}^{\text{III}}: 3d^5$).

For 3C, no further change is seen to the ATD, even after three passes, suggesting that this conformer is highly stable and does

not interconvert (Figure S14). For the extended distribution 3E, multiple passes broaden the ATD, but no further

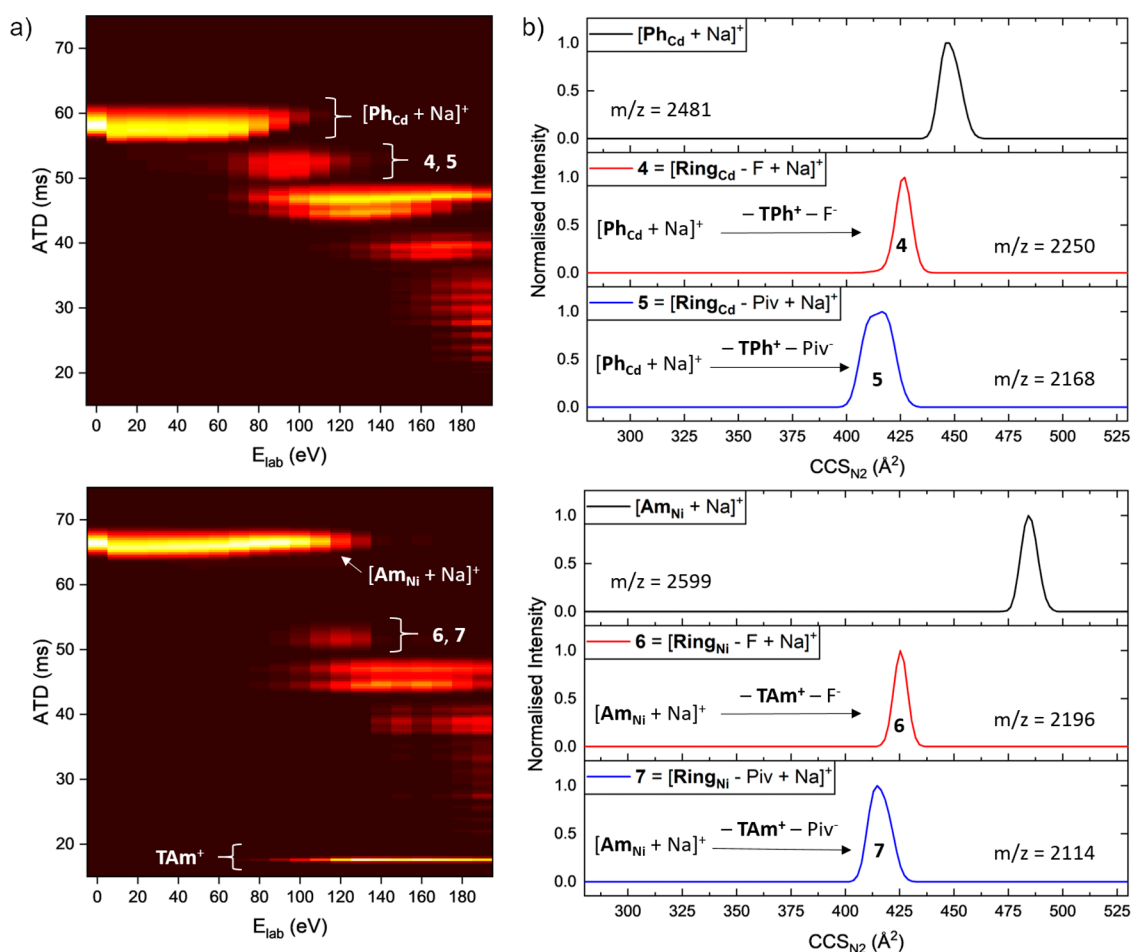


Figure 3. (a) Collision energy vs arrival time distribution heat map for $[\text{Ph}_{\text{Cd}} + \text{Na}]^+$ ($m/z = 2481$, top) and $[\text{Am}_{\text{Ni}} + \text{Na}]^+$ ($m/z = 2599$, bottom) as well as the corresponding fragments. 10 μM Ph_{Cd} and Am_{Ni} were used in 500 μM NaI and 4:1 toluene/methanol (Ph_{Cd}) or 7:3 methanol/DCM (Am_{Ni}). The intact thread cation TAm^+ was observed, whereas no TPh^+ ions could be detected (Figure S31). (b) CCS_{N_2} distributions of $[\text{Ph}_{\text{Cd}} + \text{Na}]^+$ and its fragments (4, 5) at $E_{lab} = 90$ eV (top) as well as $[\text{Am}_{\text{Ni}} + \text{Na}]^+$ and its fragments (6, 7) at $E_{lab} = 120$ eV (bottom).

resolution is achieved, indicating that this feature contains interconverting species that are conformationally dynamic on the experimental timescale (~ 250 ms, Figure S15). We also examined how collision energy influences the population of these features in the activated IM-MS spectra of $[\text{Ring}_{\text{Mn}}]^-$. For all fragments 1–3, the C distributions form and subsequently dissociate at slightly lower E_{lab} than the extended distributions E (Figure S16). DFT calculations were performed to discern the structures of the 3 conformers (Table S4), including a seven-membered Cr_6Mn -ring as a candidate for 3C (Figure S17) and different opened helical forms as candidates for 3E (Figures S18–S22). A comparison between their predicted CCS_{N_2} values with those found experimentally is instructive in understanding the disassembly processes for $[\text{Ring}_{\text{M}}]^-$ (see below).

[2]-Rotaxane Families $[\text{NH}_2\text{RR}'][\text{Ring}_{\text{M}}] = \text{Ph}_{\text{M}}$ and Am_{M} . The same workflows were applied to the rotaxane families Ph_{M} and Am_{M} , where the secondary ammonium cation $[\text{NH}_2\text{RR}']^+$ (Ph_{M} : $\text{R} = \text{CH}_2\text{Ph}$, $\text{R}' = \text{CH}_2\text{CH}_2\text{Ph}$ (“ TPh^+ ”) and Am_{M} : $\text{R} = \text{R}' = \text{C}_6\text{H}_{12}\text{NHC}(\text{O})\text{tBu}$ (“ TAm^+ ”), referred to as the thread, was postulated to not easily dissociate from the heterometallic rings $[\text{Ring}_{\text{M}}]^-$ due to the large R, R' groups (Figure 2a,b).²⁶

Disassembly and Stability Trends of the Rotaxane Ions $[\text{Ph}_{\text{M}} + \text{A}]^+$ and $[\text{Am}_{\text{M}} + \text{A}]^+$ ($\text{A}^+ = \text{H}^+, \text{Na}^+$). Ph_{M} and Am_{M}

were transferred to the gas phase from solutions of NaI and yielded protonated cations and sodiated forms $[\text{Ph}_{\text{M}} + \text{A}]^+$ and $[\text{Am}_{\text{M}} + \text{A}]^+$, among others ($\text{A}^+ = \text{H}^+, \text{Na}^+$; Figure S23 for $\text{M} = \text{Co}^{\text{II}}$, Supplementary Data Set for other M). Considerable differences are observed between their fragmentation behavior, with the sodiated forms being significantly more stable than the protonated species (Figure 2c and Figures S24–S29).

We performed a quantitative investigation of the rotaxane fragmentation and determined the E_{50} values for all ions $[\text{Ph}_{\text{M}} + \text{A}]^+$ and $[\text{Am}_{\text{M}} + \text{A}]^+$ ($\text{A}^+ = \text{H}^+, \text{Na}^+$) with $\text{M} = \text{Mn}^{\text{II}}, \text{Fe}^{\text{II}}, \text{Co}^{\text{II}}, \text{Ni}^{\text{II}}, \text{Cu}^{\text{II}}, \text{Zn}^{\text{II}}, \text{Cd}^{\text{II}}$ (Table S1 and Figure 2c), as well as for $[\text{Ph}_{\text{Fe}(\text{III})}]^+$ and $[\text{Am}_{\text{Fe}(\text{III})}]^+$, which showed the same disassembly pathway (Figure S30). The results demonstrate that three factors influence the stability of the rotaxane ions $[\text{Ph}_{\text{M}} + \text{A}]^+$ and $[\text{Am}_{\text{M}} + \text{A}]^+$: first, the metal M in the heterometallic ring and its oxidation state, second, the thread and its end group (TPh^+ vs TAm^+), and finally, the charge carrying species A^+ ($\text{A}^+ = \text{H}^+, \text{Na}^+$), where we observed a significant difference between protonated species and sodiated forms. The impact of these and other charge carriers on the disassembly, stability, and conformations of these complexes is the subject of another report.²⁸

Ion Mobility Investigations of the Rotaxane Ions $[\text{Ph}_{\text{M}} + \text{Na}]^+$, $[\text{Am}_{\text{M}} + \text{Na}]^+$ and Their Fragments. We use the same activated ion-mobility workflow as for $[\text{Ring}_{\text{M}}]^-$ to consider by

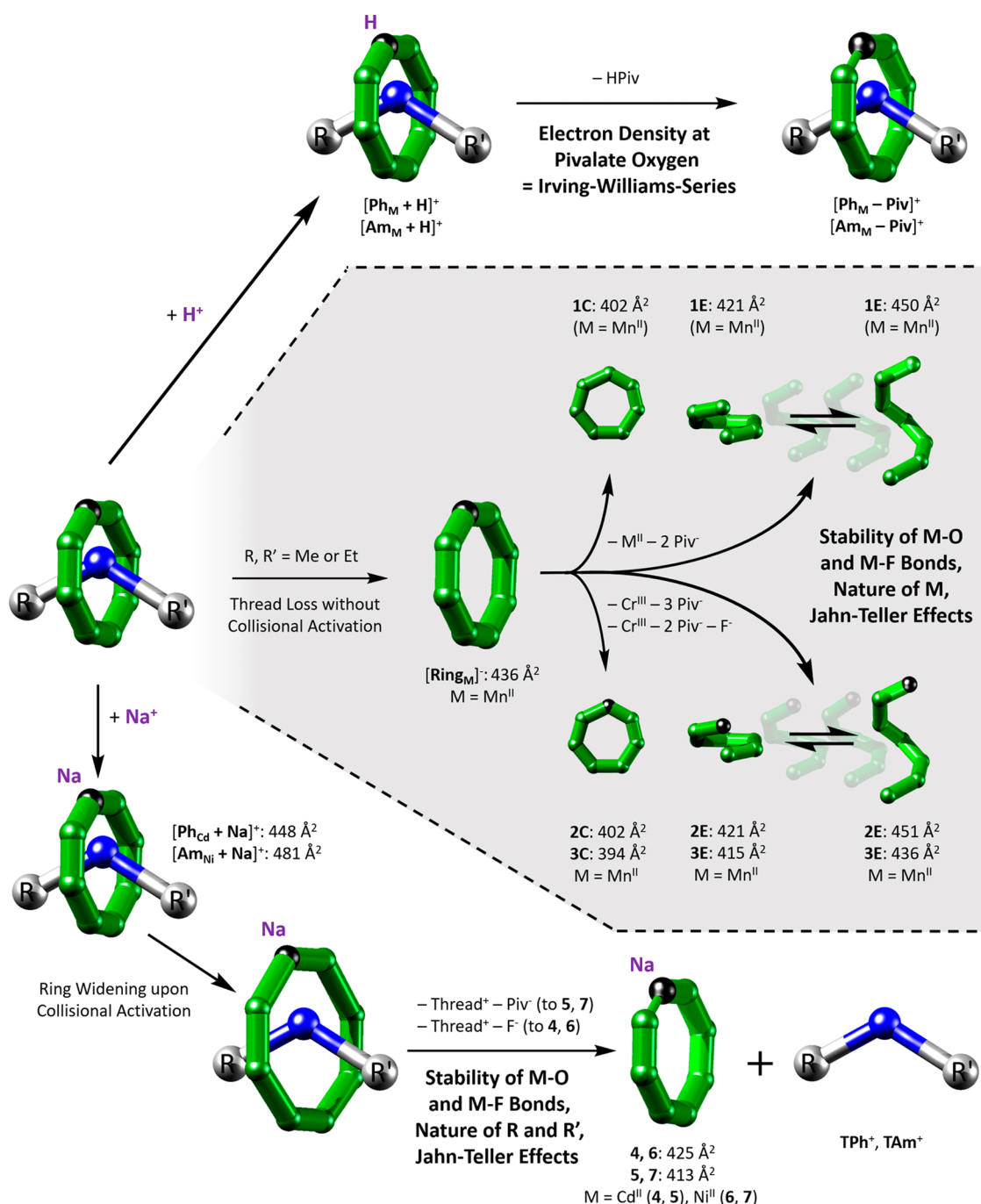


Figure 4. Disassembly of $[\text{Ring}_M]^-$, $[\text{Ph}_M + \text{A}]^+$ and $[\text{Am}_M + \text{A}]^+$ ($\text{A}^+ = \text{H}^+, \text{Na}^+$) including fragmentation channels, determining stability factors, and CCS_{N_2} (Cr: green, M: black, N: blue, Rest: white). Top: suggested loss of pivalic acid adjacent to M for the protonated species $[\text{Ph}_M + \text{H}]^+$ and $[\text{Am}_M + \text{H}]^+$. Center: predicted conformations of $[\text{Ring}_M]^-$ fragments 1–3 involving interconverting helical structures E and closed rings C. CCS_{N_2} values are given for $\text{M} = \text{Mn}^{\text{II}}$. ATD for other d-metals are found in the [Supporting Information](#) and the supplementary data set. Bottom: observed slipping mechanism for the sodiated forms $[\text{Ph}_M + \text{Na}]^+$ and $[\text{Am}_M + \text{Na}]^+$ including ring widening, showing the intact ring fragments 4–7 in the activated IM-MS spectra.

what route the thread detaches from the ring in the sodiated forms. Examples of $[\text{Ph}_{\text{Cd}} + \text{Na}]^+$ and $[\text{Am}_{\text{Ni}} + \text{Na}]^+$ are presented (Figure 3), although other species were also examined and qualitatively show the same behavior (Supporting Data Set).

The heat maps in Figure 3a illustrate the collision induced fragmentation of $[\text{Ph}_{\text{Cd}} + \text{Na}]^+$ (top) and $[\text{Am}_{\text{Ni}} + \text{Na}]^+$ (bottom) *via* changes in arrival time distribution. The dissociation of the rotaxane species occurs at different energies,

with $[\text{Am}_{\text{Ni}} + \text{Na}]^+$ being significantly more stable than $[\text{Ph}_{\text{Cd}} + \text{Na}]^+$ (Figure 2c). Both precursor ions show similar behavior to $[\text{Ring}_M]^-$ (Figure S10a) with no major structural change.

As discussed before, the fragmentation channels are similar for both ions and involve the loss of the thread and one anionic ligand (F^- : 4, 6 and Piv^- : 5, 7). The ATD of the precursor ions $[\text{Ph}_{\text{Cd}} + \text{Na}]^+$ and $[\text{Am}_{\text{Ni}} + \text{Na}]^+$ as well as their direct fragments 4–7 were converted to CCS_{N_2} (Figure 3b), showing that $[\text{Am}_{\text{Ni}} + \text{Na}]^+$ is 9% larger than $[\text{Ph}_{\text{Cd}} + \text{Na}]^+$ due to the

size of the thread end groups. Fragments 4–7 have very close CCS_{N_2} values, with 5 and 7 being only slightly smaller than 4 and 6. Fragments 4, 6, and 7 are unimodal, whereas 5 indicates two closely related conformers; however, none exhibit the conformational diversity shown for the fragments of $[\text{Ring}_{\text{Mn}}]^-$ (Figure 1b). The small CCS_{N_2} differences between the two fragmentation channels occur because of the number of bulky pivalate ligands present (4, 6: 16 Piv⁻; 5, 7: 15 Piv⁻), whereas the asymmetric peak shapes of 5 and 7 are possibly attributable to pivalate loss from different coordination sites, either in or perpendicular to the metal plane.

DISCUSSION

Disassembly and Stability Trends. Heterometallic Rings $[\text{Ring}_{\text{M}}]^-$. The trends in E_{50} values for $[\text{Ring}_{\text{M}}]^-$ (Figure 1d, Table S1) can be explained by considering the varying strengths of M–O and M–F bonds and the effective nuclear charge at the metal centers (Figure 4 center). The increased stability from Mn^{II} (3d⁵) to Ni^{II} (3d⁸) is attributable to the increasing effective nuclear charge and occupation of the stabilizing t_{2g} -orbitals in the octahedral crystal field. For Cu^{II}, Zn^{II}, and Cd^{II}, the reverse trend would be expected due to occupation of the destabilizing e_g -orbitals and for Cd^{II} because of a larger ionic radius (Zn^{II} vs Cd^{II}, Figure 1d and Table S1). Small deviations from this trend are shown by Mn^{II}, which we would predict to be less stable than Fe^{II} (3d⁵ vs 3d⁶), and also by Cu^{II}, which should be more stable than Zn^{II} (3d⁹ vs 3d¹⁰). We suggest that the repulsive forces between the pivalate ligands are less in $[\text{Ring}_{\text{Mn}}]^-$ than for the other rings because of the larger ionic radius for Mn^{II}, compensating for the smaller Mn^{II}–O bond energy.³⁰ The lability of $[\text{Ring}_{\text{Cu}}]^-$ is a result of Jahn–Teller distortions causing the elongation of one of the F–Cu^{II}–O axes,³¹ which is well-known from other Cu^{II} complexes and its impact on periodic stability trends previously reported.^{32,33} Jahn–Teller effects could also make $[\text{Ring}_{\text{Cu}}]^-$ more flexible, as observed before for related containing five-coordinate Cu^{II} sites.³⁴ Notably, our data agree well with the M^{II} trend for water-exchange reaction rate constants of the hexaaqua ions $[\text{M}^{\text{II}}(\text{H}_2\text{O})_6]^{2+}$ (Table S5, Figure S32), although a different stability trend from ESI-MS experiments has recently been reported for supramolecular terpyridine-based fractal complexes (Ni^{II} > Co^{II} > Zn^{II} > Fe^{II} > Cu^{II} > Cd^{II} > Mn^{II}), indicating that the electronic environment of M^{II} may be altered in the case of some ligands.³⁵

Sodiated Rotaxane Ions $[\text{Ph}_{\text{M}} + \text{Na}]^+$ and $[\text{Am}_{\text{M}} + \text{Na}]^+$. The loss of the thread must involve significant disruption of the ring, perhaps complete opening. This process would certainly involve lengthening or even breaking M^{II}–O and M^{II}–F, or less likely Cr^{III}–O and Cr^{III}–F bonds. We find a similar trend in stability, with respect to M^{II}, for the sodiated species $[\text{Ph}_{\text{M}} + \text{Na}]^+$ and $[\text{Am}_{\text{M}} + \text{Na}]^+$ (Figures 2b and 4 bottom) to the data of the heterometallic ring anions $[\text{Ring}_{\text{M}}]^-$ (Figure 1d). Again, the trend agrees with water-exchange reaction rate constants of the hexaaqua ions $[\text{M}^{\text{II}}(\text{H}_2\text{O})_6]^{2+}$ (Figure S33). A difference between the metal trends of the sodium adducts and the ring anions are the species with M = Zn^{II} and Cd^{II}, where we observe a higher stability for M = Cd^{II} in both. Cd^{II} is the only 4d metal in this study and its bigger size and lower charge density might lead to a more favorable chelation of the sodium cation and/or stronger H–F hydrogen bonds in the thread resulting from weaker Cd^{II}–F bonds.

The thread and its functionality have a significant impact on the E_{50} values of the sodiated ions $[\text{Ph}_{\text{M}} + \text{Na}]^+$ and $[\text{Am}_{\text{M}} +$

$\text{Na}]^+$ (Figures 2b and 4 bottom, Table S1). The ions $[\text{Am}_{\text{M}} + \text{Na}]^+$ are all more stable than $[\text{Ph}_{\text{M}} + \text{Na}]^+$, which can be attributed to both steric and electronic effects. The *tert*-butyl groups in TAm^+ are larger than the phenyl end groups in TPh^{+36} , making it harder for the thread to dissociate from the ring. Further, the amide end groups will form stronger charge–charge interactions with the macrocycle than the phenyl groups, making $[\text{Am}_{\text{M}} + \text{Na}]^+$ more stable. We also examined $[\text{Ph}_{\text{Fe(III)}}]^+$ and $[\text{Am}_{\text{Fe(III)}}]^+$ (Figure S30), which allows us to consider the effect of oxidation state when compared to the divalent metals M^{II}. These exhibit strongly enhanced stabilities resulting from stronger charge–charge interactions of Fe^{III} and the absence of an additional cation, which presumably weakens the M–O and M–F bonds (Figure 2c).

Protonated Rotaxane Ions $[\text{Ph}_{\text{M}} + \text{H}]^+$ and $[\text{Am}_{\text{M}} + \text{H}]^+$. The fragmentation of the protonated rotaxane ions takes place at significantly lower E_{50} values (Figure 2c) than the sodiated forms and also leads to a different fragmentation pathway, which always involves the loss of one pivalic acid (Figure S24). Protonation followed by pivalic acid dissociation is more likely on a carboxylate oxygen bound to M^{II} than one adjacent to Cr^{III} due to higher charge density on the O-donor, which is why the E_{50} values of $[\text{Ph}_{\text{M}} + \text{H}]^+$ and $[\text{Am}_{\text{M}} + \text{H}]^+$ depend also on the divalent metal M^{II} (Figure 4 top). The E_{50} trend agrees well with the Irving–Williams series across the measured 3d-metal rings,⁴¹ with the exception of Cd^{II} which is not part of the Irving–Williams series as it is a 4d metal and shows a smaller E_{50} value than Zn^{II} (both d¹⁰). This is presumably because of its larger size that destabilizes the M^{II}–O bond (Table S1). Another interesting correlation occurs with the pK_{A} values of the hexaaqua ions $[\text{M}^{\text{II}}(\text{H}_2\text{O})_6]^{2+}$ (Figure S34). The significantly lower E_{50} values of $[\text{Ph}_{\text{M}} + \text{H}]^+$ and $[\text{Am}_{\text{M}} + \text{H}]^+$ compared to the sodium adducts suggest a strong involvement of the proton, weakening the M–O bond significantly. As the metal with the lowest pK_{A} ³⁷ (M = Cu^{II}) in $[\text{M}^{\text{II}}(\text{H}_2\text{O})_6]^{2+}$ forms the weakest O–H and hence the strongest M–O bond, $[\text{Ph}_{\text{Cu}} + \text{H}]^+$ and $[\text{Am}_{\text{Cu}} + \text{H}]^+$ are expected to show the highest E_{50} values. This was confirmed by our experimental data and the complete correlation with the pK_{A} trend of the hexaaqua ions, as shown in Figure S34.

Ion Mobility Investigations and DFT Studies. Heterometallic Rings $[\text{Ring}_{\text{M}}]^-$. Activated ion mobility analysis of $[\text{Ring}_{\text{Mn}}]^-$ shows that the conformation is largely unaltered until fragmentation (Figure S10a). The ATD for each fragment are diagnostic and support disassembly into two conformational forms: a compact, rigid species C and an extended, flexible species E (Figure 1b). The relative intensities of the bimodal ATD found for product ions 1–3 alter with the number of pivalate ligands. For 1 and 2, the metal centers proximal to the cleavage point now possess two pivalate groups and repulsive interactions between these bulky ligands could lead to the preference of extended conformations (1E and 2E: $\text{CCS}_{\text{N}_2} \approx 412\text{--}463 \text{ \AA}^2$, Figure 1b). Conversely, 3 has only one remaining pivalate ligand at the cleavage point, which could preferentially rearrange to be closer to the metal center, resulting in a more contracted conformation (3C: $\text{CCS}_{\text{N}_2} = 394 \text{ \AA}^2$). IMS² experiments on the extended species 3E did not provide any better separation after multiple passes in the cyclic drift ring, indicating that 3E contains a dynamic equilibrium of interconverting conformers (Figure S15).

The collected data suggest that two disassembly mechanisms occur for $[\text{Ring}_{\text{M}}]^-$ (Figure 4 center), depending on both M (Figures S11–S13) and the collision energy (Figure S16). The

metals with smaller E_{50} values, namely, Cu^{II} , Zn^{II} , and Cd^{II} (Figure 1d), have a stronger tendency to form **1** over **2** and **3** and also to yield **1C** over **1E**. This argues that this low energy mechanism leads only to minor ring disruption, favoring retention of compact conformers **C**. For the divalent metals with higher E_{50} values, more **1E** is seen, indicating a greater perturbation of the structure. The fact that Cu^{II} , Zn^{II} , and Cd^{II} decompose more to **C** than the other metals can be explained with their size (Cd^{II}) and their tendency to form complexes with lower coordination numbers, facilitating the departure of the metal center without major ring disruption. Surprisingly, the divalent metal **M** in the precursor $[\text{Ring}_\text{M}]^-$, influences the conformations seen for the main fragment **1**, despite **1** only containing chromium (Figures S11–S13). This strongly suggests that the stability of the leaving group $\{\text{MPiv}_2\}$, and the ease with which it can depart, is a driving factor for the preference of **C** or **E**, agreeing with the relative preference of Cu^{II} , Zn^{II} , and Cd^{II} for tetrahedral coordination geometries.

We hypothesize that the contracted conformers **C** are seven-membered rings (Figure 4 center), which have been reported once previously, for a Cr_6Ce ring where the large ionic radius of the heterometal was crucial.³⁸ Such species, assuming a similar connectivity as for $[\text{Ring}_\text{M}]^-$, can most easily form when exactly three ligands are present per metal center as in **2** and **3**, which would explain the preference for **1E** over **1C**. The broader peaks at higher CCS_{N_2} could correspond to extended horseshoe structures with seven metal centers, which are more common than the closed seven-membered rings in solution.³⁹

Informed by the structures obtained from DFT and their predicted CCS_{N_2} , we can rationalize the disassembly process of $[\text{Ring}_{\text{Mn}}]^-$. On the basis of systematic differences for each $[\text{Ring}_\text{M}]^-$, we apply a scaling factor of 0.92 to all predicted CCS_{N_2} values for hypothetical fragment structures of **3** (Table S4). These scaled $\text{CCS}_{\text{N}_2(s)}$ values of a Cr_6Mn -ring (Figure S17) and a slightly opened helix (Figure S20) agree well with the experimental CCS_{N_2} of **3C**, suggesting that only minor ring perturbation takes place. By contrast, the $\text{CCS}_{\text{N}_2(s)}$ of the more open helical conformers (Figures S21 and S22) are in the experimental CCS_{N_2} range of **3E**, agreeing with our predictions that these are highly disrupted opened ring structures.

Sodiated Rotaxane Ions $[\text{Ph}_\text{M} + \text{Na}]^+$ and $[\text{Am}_\text{M} + \text{Na}]^+$. The disassembly of the sodiated rotaxanes involves the loss of the thread (TPH^+ or TAM^+), for which two mechanisms can be considered. The first proceeds by an opening of the ring structure followed by thread release, and the second proceeds by a slipping mechanism through the cavity of the ring. The latter is relatively small for $[\text{Ring}_\text{M}]^-$ compared to common organic macrocycles, largely because of the bulky pivalate ligands, and $[\text{Ring}_\text{M}]^-$ therefore appears to hold the thread even with small stopper groups such as in TPH^+ and TAM^+ (Figure 2b). Space-filling models of the crystal structures Ph_{Cd} and Am_{Ni} ²⁹ suggest that the cavity of the ring (diameter ≈ 3.5 Å) and the R and R' groups (width ≈ 5.8 – 5.9 Å) will not permit a slipping mechanism (Figures S35 and S36, Table S6). We previously studied the kinetic stability of Am_{Co} , where we added a similar, isotopically labeled rotaxane at 60 °C. No ring or thread exchange occurred between the molecules after stirring the solution for one week.²⁹ These data did not point to a slipping mechanism for disassembly in solution, but ambiguity in the analysis from new bulk phase measurements warranted further investigation.

The observed gas phase stability trends for $[\text{Ph}_\text{M} + \text{Na}]^+$ and $[\text{Am}_\text{M} + \text{Na}]^+$ (Figure 2c) are similar to the one obtained for

the $[\text{Ring}_\text{M}]^-$ series (Figure 1d) as the stability of **M–O** and **M–F** bonds likely determines the E_{50} value here as well. This can be due to either bond breaking or lengthening and does not help to determine the dethreading mechanism. The evidence from ion mobility measurements is more useful, and following thread loss, the rotaxane ring fragments (**4**–**7**) present have narrow ATD, indicative of compact structures with no evidence of extended conformers as seen for $[\text{Ring}_{\text{Mn}}]^-$ (Figure 1b). In the ion mobility heat maps of $[\text{Ph}_{\text{Cd}} + \text{Na}]^+$ and $[\text{Am}_{\text{Ni}} + \text{Na}]^+$ (Figure 3a), the observed precursor ATD narrows between $E_{\text{lab}} = 60$ – 90 eV, which suggests minimal disruption of the ring structure prior to the loss of thread.

Our hypothesis, therefore, that the ring has widened prior to thread release is further strengthened by comparison of the CCS_{N_2} distributions of fragments **4** and **6** (Figure 3b) with corresponding $[\text{Ring}_\text{M}]^-$ anions (Figure 1b), where we find highly similar experimental CCS_{N_2} values for the rotaxane ring fragment ions $[(\text{Ring}_\text{M} - \text{F}) + \text{Na}]^+$ (**4**, **6**) after the thread has been lost. As we assign the $[\text{Ring}_\text{M}]^-$ ions as closed rings, we attribute a slipping mechanism to the fragmentation of the sodiated forms $[\text{Ph}_\text{M} + \text{Na}]^+$ and $[\text{Am}_\text{M} + \text{Na}]^+$ (Figure 4 bottom), although ring opening followed by thread release and fast reclosing of the ring is also possible. The almost identical CCS_{N_2} values of the fragments **4**, **6** and **5**, **7** (Figure 3b) can be explained by their nearly equal composition (only difference in **M**) and strongly implies that the same dethreading mechanism occurs for both ions $[\text{Am}_{\text{Ni}} + \text{Na}]^+$ and $[\text{Ph}_{\text{Cd}} + \text{Na}]^+$. Considering that the thread end groups in both Am_M and Ph_M are significantly larger than the ring diameter, as shown by space-filling models from the crystal structures (Figures S35 and S36, Table S6), this result is noteworthy and warrants further investigation.

CONCLUSIONS

We have shown that energy-resolved MS^2 and IM- MS coupled with DFT combine effectively to characterize polymetallic complexes in the gas-phase, yielding information on the compounds' disassembly, energetics, and conformational dynamics. Our study demonstrates that these methods, more commonly applied to the disassembly of protein complexes,^{6,40–43} can be usefully applied for supramolecular and inorganic chemistry. The results show that the stability of the studied ring and rotaxane ions is tuned by altering the d-metal composition in the heterometallic ring, the end groups in the thread, and the charge carrying ion, providing a framework to follow in for the future design of self-assembled polymetallic complexes.

IM- MS was applied to investigate the dissociation mechanism of the rotaxane ions in the gas phase, suggesting that the thread slips through the cavity of the ring after bond lengthening near **M**. Examination of the $[\text{Ring}_\text{M}]^-$ disassembly with IM- MS disclosed two mechanistic routes, leading to compact seven-membered rings as well as conformationally dynamic open horseshoes. Perhaps most curiously, we find that the structure of the homometallic fragment **1** = $[\text{Cr}_7\text{F}_8\text{Piv}_{14}]^-$ is differentiated into compact or extended product ions depending on the divalent metal in the precursor ion, even though **M** is no longer present.

For all studied species, the trends in stability and ensuing disassembly mechanisms can be rationalized using concepts from crystal field theory, demonstrating that classic observations such as Jahn–Teller effects and the Irving–Williams series

are applicable to large polymetallic compounds. Extending this to include ligand field theory would suggest other factors such as interelectronic repulsion (the nephelauxetic effect), spin-orbit coupling and variation in bond lengths could be evaluated.⁴⁴ In the future, it may be possible to compare the simple crystal field theory explanation here with a more sophisticated ligand field theory approach. For now, we conclude that the use of IM-MS coupled with *ab initio* calculations to examine (metallo-)supramolecular complexes has considerable promise.¹³

EXPERIMENTAL/METHODS

Synthesis and Materials. The rotaxanes Am_M ($M = \text{Mn}^{\text{II}}, \text{Fe}^{\text{II}}, \text{Co}^{\text{II}}, \text{Ni}^{\text{II}}, \text{Cu}^{\text{II}}, \text{Zn}^{\text{II}}, \text{Cd}^{\text{II}}$)²⁹ and $[\text{NH}_2(\text{CH}_3)_2][\text{Ring}_M]$ ($M = \text{Mn}^{\text{II}}, \text{Co}^{\text{II}}, \text{Ni}^{\text{II}}, \text{Cu}^{\text{II}}, \text{Zn}^{\text{II}}, \text{Cd}^{\text{II}}$)^{34,45} as well as $[\text{NH}_2(\text{C}_2\text{H}_5)_2][\text{Ring}_{\text{Fe}}]$ ⁴⁵ were prepared using methods previously reported by our group. The rotaxane family Ph_M ($M = \text{Mn}^{\text{II}}, \text{Fe}^{\text{II}}, \text{Co}^{\text{II}}, \text{Ni}^{\text{II}}, \text{Cu}^{\text{II}}, \text{Zn}^{\text{II}}, \text{Cd}^{\text{II}}$) and the corresponding secondary amine (deprotonated form of TPh^+) were synthesized according to experimental procedures described in the SI (Figure S37). Crystal structures were obtained for Ph_M ($M = \text{Mn}^{\text{II}}, \text{Fe}^{\text{II}}, \text{Co}^{\text{II}}, \text{Ni}^{\text{II}}, \text{Cu}^{\text{II}}, \text{Zn}^{\text{II}}, \text{Cd}^{\text{II}}$, Figures S38–S44, Table S7).

All reagents and solvents were purchased from Sigma-Aldrich, Alfa, Fisher Scientific, or Fluorochem and used without further purification. The syntheses of the hybrid organic–inorganic rotaxanes were carried out in Erlenmeyer Teflon FEP flasks supplied by Fisher Scientific. Column chromatography was performed using either 40–63 μm silica from Sigma-Aldrich or a Grace Reverelis X2 Autocolumn with Grace Reverelis NP cartridges.

Sample Preparation. Samples were typically prepared in 500 μM NaI and 7:3 methanol/toluene (Am_M) or 4:1 toluene/methanol (Ph_M , $[\text{NH}_2(\text{CH}_3)_2][\text{Ring}_M]$, $[\text{NH}_2(\text{C}_2\text{H}_5)_2][\text{Ring}_{\text{Fe}}]$) respectively. Concentrations of 2 μM (Q Exactive UHMR) and 10 μM (Cyclic IMS) were typically used. When necessary, 0.5–1% formic acid was added to enhance the signal of the protonated ions. For the activated ion mobility data of $[\text{Ring}_{\text{Cd}}]^+$, a sample of Am_{Cd} was used instead of $[\text{NH}_2(\text{CH}_3)_2][\text{Ring}_{\text{Cd}}]$.

Mass Spectrometry (MS) and Ion-Mobility Mass Spectrometry (IM-MS). All samples were ionized with a nanoESI source and sprayed from borosilicate glass capillaries (World Precision Instruments, Stevenage, UK), which were pulled on a Flaming/Brown P-2000 laser puller (Sutter Instrument Company, Novato, CA, US). A potential of 1.0–1.5 kV was applied through a platinum wire (diameter = 0.125 mm, Goodfellow, Huntingdon, UK) inserted into the nanoESI capillaries. The source temperature was set to 23° (Cyclic IMS) and 30° (Q Exactive UHMR), respectively.

The Q Exactive ultra-high mass range (UHMR) hybrid quadrupole-Orbitrap mass spectrometer (Thermo Fisher)⁴⁶ was used for the derivation of all E_{50} values *via* tandem mass spectrometry (MS^2) experiments involving collision-induced dissociation (CID) studies. The complete isotopic envelope of the target ions were typically m/z -selected in a quadrupole filter, accelerated to a determined kinetic energy (E_{lab} : 0–300 eV) and subsequently injected into the high-energy C-trap dissociation (HCD) cell, which contained nitrogen gas at a constant pressure (trapping gas pressure parameter: 2.0). Fragment ions as well as precursor ions that did not fragment, were mass-analyzed in the Orbitrap mass analyzer (resolution: 25000, AGC target: 3E6 ions, maximum inject time: 100 ms).

Ion mobility mass spectrometry (IM-MS) experiments were performed on a Select Series Cyclic IMS (Waters).⁴⁷ After the transfer to the gas phase (cone voltage: 20–60 V, source offset: 10–20 V, purge gas: 50–300 L/h), ions of interest were isolated by a quadrupole mass filter, activated in a trap cell where appropriate (trap bias: 2 V, E_{lab} : 0–200 eV) and subsequently injected into the cyclic ion mobility drift ring. In this region, ions were separated by using a nonuniform electric field under a constant nitrogen pressure. Traveling waves (TW, height: 20 V) pushed the ions through the cyclic drift region. Unless noted otherwise, ions traveled one pass in the cyclic drift ring (“single path”, separation time: 2 ms) and were

subsequently transferred (transfer energy: 4–15 V) to a time-of-flight mass analyzer. Details of this method known as traveling-wave ion mobility spectrometry (TWIMS) can be found elsewhere.^{3,48–50}

Data Processing. Mass spectra were recorded for different kinetic energies, and the survival yield (SY) of each precursor ion was calculated from its absolute intensity (I_p) and the sum of the fragment ion intensities (I_f) according to eq 1:

$$\text{SY} = \frac{I_p}{I_p + \sum I_f} \quad (1)$$

Additionally, laboratory kinetic energies E_{lab} were converted to center-of-mass energies E_{com} using eq 2. This relationship assumes a single collision of the stationary target gas with the mass m_g for this work nitrogen, with the accelerated precursor ion of the mass m_p . Under these conditions, the maximum amount of kinetic energy accessible for the conversion to internal energy is given by E_{com} .^{51,52}

$$E_{\text{com}} = \frac{m_g}{m_g + m_p} \times E_{\text{lab}} \quad (2)$$

The center-of-mass energy where $\text{SY} = 0.5$ (or 50%) can be defined as E_{50} , which is known as a relative measure of precursor ion stability in the gas phase. Experimental parameters (trapping gas pressure, temperature, and pre-CID voltages) are maintained constant in order to obtain comparable and meaningful E_{50} values across different precursor ions; however comparisons across different instruments are not trivial.⁵² E_{50} values are derived from plots of SY vs E_{com} by using a fit with a sigmoidal Hill function (Hill1 function in OriginPro 2020b). For some of the studied protonated forms, contaminating species overlapped and showed significantly different stabilities. In these cases, the share of the contamination was subtracted in the survival yield plots before fitting.

Activated ion mobility mass spectrometry data obtained from a Select Series Cyclic IMS instrument (Waters) were not converted to E_{com} . Experimentally obtained arrival time distributions were converted to nitrogen collisional cross sections ($^{\text{TW}}\text{CCS}_{\text{N}_2}$, $\text{TW} = \text{“Traveling Waves”}$) *via* published calibration procedures.⁵³ The Agilent tune mix was used for all $^{\text{TW}}\text{CCS}_{\text{N}_2}$ calibrations.⁵⁴

Density Functional Theory and Collision Cross Section Calculations. All DFT calculations were carried out with Gaussian 16⁵⁵ utilizing the B3LYP exchange-correlation functional with the Grimme D3 empirical dispersion correction.⁵⁶ An effective core potential and its associated split valence basis set were used for transition metals (LANL2DZ),⁵⁷ and a 6-31G(d) basis set on other atoms. All structures were optimized to the default convergence criteria (RMS force $< 3 \cdot 10^{-4}$ E_h/a_0), and the conformers were confirmed to be the minima by vibrational analysis with corresponding formate models (O_2CH^- instead of $\text{O}_2\text{C}^-\text{Bu}$). Metal electronic states were high spin, as found experimentally, with low deviations from $\langle S^2 \rangle$ although they were ferromagnetically coupled. Atomic charges were obtained for the optimized structures at the same DFT level using the Merz–Kollman method with UFF-based radii as implemented in Gaussian 16.

Theoretical collision cross section values ($^{\text{TH}}\text{CCS}_{\text{N}_2}$, $\text{TH} = \text{“Theoretical”}$) were obtained from the software IMoS by using the trajectory method in nitrogen gas including quadrupole potential (number of orientations: 3, gas molecules per orientation: 300,000, temperature: 298 K, pressure: 101,325 Pa = 1 atm).²⁷

Crystallographic Data. Single crystal XRD data was collected on an Agilent SuperNova CCD diffractometer with Mo $K\alpha$ radiation ($\lambda = 0.71073 \text{ \AA}$) and a Rigaku FR-X with Cu $K\alpha$ radiation ($\lambda = 1.5418 \text{ \AA}$) equipped with a Hypix6000HE detector. Data was measured using the CrysAlisPro suite of programs⁵⁸ and was solved using the SHELXL and Olex 2 suite of programs.^{59,60}

ASSOCIATED CONTENT

Data Availability Statement

The supplementary data set is available on Figshare 10.6084/m9.figshare.20324448 and contains the raw ion mobility mass

spectrometry and mass spectrometry data files as well as the outputs from DFT calculations.

SI Supporting Information

The Supporting Information is available free of charge at <https://pubs.acs.org/doi/10.1021/jacs.2c07522>.

Mass spectrometry, tandem mass spectrometry, and ion mobility mass spectrometry data of $[\text{Ring}_M]^-$, $[\text{Ph}_M + \text{A}]^+$, and $[\text{Am}_M + \text{A}]^+$ as well as related data; density functional theory studies and predicted collision cross sections of $[\text{Ring}_M]^-$, its conformers and of fragment 3; crystal data and studies of Ph_M and Am_M ; synthetic procedure for Ph_M (PDF)

Accession Codes

CCDC 2176287–2176293 contain the supplementary crystallographic data of Ph_M . These data can be obtained free of charge via www.ccdc.cam.ac.uk/data_request/cif, or by emailing data_request@ccdc.cam.ac.uk, or by contacting The Cambridge Crystallographic Data Centre, 12 Union Road, Cambridge CB2 1EZ, UK; fax: +44 1223 336033.

AUTHOR INFORMATION

Corresponding Author

Perdita E. Barran – Michael Barber Centre for Collaborative Mass Spectrometry, Department of Chemistry, Manchester Institute of Biotechnology, The University of Manchester, Manchester M1 7DN, U.K.; orcid.org/0000-0002-7720-586X; Email: perdita.barran@manchester.ac.uk

Authors

Niklas Geue – Michael Barber Centre for Collaborative Mass Spectrometry, Department of Chemistry, Manchester Institute of Biotechnology, The University of Manchester, Manchester M1 7DN, U.K.; orcid.org/0000-0002-5216-8353

Tom S. Bennett – Department of Chemistry, The University of Manchester, Manchester M13 9PL, U.K.

Alexandra-Ana-Maria Arama – Department of Chemistry, The University of Manchester, Manchester M13 9PL, U.K.

Lennart A. I. Ramakers – Michael Barber Centre for Collaborative Mass Spectrometry, Department of Chemistry, Manchester Institute of Biotechnology, The University of Manchester, Manchester M1 7DN, U.K.

George F. S. Whitehead – Department of Chemistry, The University of Manchester, Manchester M13 9PL, U.K.; orcid.org/0000-0003-1949-4250

Grigore A. Timco – Department of Chemistry, The University of Manchester, Manchester M13 9PL, U.K.

P. B. Armentrout – Department of Chemistry, University of Utah, Salt Lake City, Utah 84112, United States; orcid.org/0000-0003-2953-6039

Eric J. L. McInnes – Department of Chemistry, The University of Manchester, Manchester M13 9PL, U.K.; orcid.org/0000-0002-4090-7040

Neil A. Burton – Department of Chemistry, The University of Manchester, Manchester M13 9PL, U.K.

Richard E. P. Winpenny – Department of Chemistry, The University of Manchester, Manchester M13 9PL, U.K.; orcid.org/0000-0002-7101-3963

Complete contact information is available at:

<https://pubs.acs.org/doi/10.1021/jacs.2c07522>

Notes

The authors declare no competing financial interest.

ACKNOWLEDGMENTS

N.G. is grateful for funding through the President's Doctoral Scholar Award by The University of Manchester. We acknowledge the support of EPSRC through the strategic equipment award EP/T019328/1, the European Research Council for funding the MS SPIDOC H2020-FETOPEN-1-2016-2017-801406, and Waters Corporation for their continued support of mass spectrometry research within the Michael Barber Centre for Collaborative Mass Spectrometry. R.E.P.W. thanks the EPSRC for an Established Career Fellowship (EP/R011079/1) and the European Research Council for an Advanced Grant (ERC-2017-ADG-786734). P.B.A. thanks the National Science Foundation, Grant CHE-1954142 for support. The authors would like to acknowledge the assistance given by Research IT and the use of the Computational Shared Facility at The University of Manchester. The authors also thank EPSRC for funding an X-ray diffractometer (EP/K039547/1) as well as the staff in the MS and Separation Science and the XRD Facilities in the Faculty of Science and Engineering, The University of Manchester, for their assistance.

REFERENCES

- (1) Lanucara, F.; Holman, S. W.; Gray, C. J.; Evers, C. E. The Power of Ion Mobility-Mass Spectrometry for Structural Characterization and the Study of Conformational Dynamics. *Nat. Chem.* **2014**, *6*, 281–294.
- (2) Dodds, J. N.; Baker, E. S. Ion Mobility Spectrometry: Fundamental Concepts, Instrumentation, Applications, and the Road Ahead. *J. Am. Soc. Mass Spectrom.* **2019**, *30*, 2185–2195.
- (3) Gabelica, V.; Shvartsburg, A. A.; Afonso, C.; Barran, P.; Benesch, J. L. P.; Bleiholder, C.; Bowers, M. T.; Bilbao, A.; Bush, M. F.; Campbell, J. L.; Campuzano, I. D. G.; Causon, T.; Clowers, B. H.; Creaser, C. S.; De Pauw, E.; Far, J.; Fernandez-Lima, F.; Fjeldsted, J. C.; Giles, K.; Groessl, M.; Hogan, C. J.; Hann, S.; Kim, H. I.; Kurulugama, R. T.; May, J. C.; McLean, J. A.; Pagel, K.; Richardson, K.; Ridgeway, M. E.; Rosu, F.; Sobott, F.; Thalassinou, K.; Valentine, S. J.; Wyttenbach, T. Recommendations for Reporting Ion Mobility Mass Spectrometry Measurements. *Mass Spectrom. Rev.* **2019**, *38*, 291–320.
- (4) Gabelica, V. Ion Mobility–Mass Spectrometry: An Overview. In *Ion Mobility-Mass Spectrometry: Fundamentals and Applications*; The Royal Society of Chemistry, 2022; pp. 1–25.
- (5) Benesch, J. L. P.; Ruotolo, B. T.; Simmons, D. A.; Robinsons, C. V. Protein Complexes in the Gas Phase: Technology for Structural Genomics and Proteomics. *Chem. Rev.* **2007**, *107*, 3544–3567.
- (6) Zhou, M.; Wysocki, V. H. Surface Induced Dissociation: Dissecting Noncovalent Protein Complexes in the Gas Phase. *Acc. Chem. Res.* **2014**, *47*, 1010–1018.
- (7) Pacholarz, K. J.; Barran, P. E. Distinguishing Loss of Structure from Subunit Dissociation for Protein Complexes with Variable Temperature Ion Mobility Mass Spectrometry. *Anal. Chem.* **2015**, *87*, 6271–6279.
- (8) Eldrid, C.; Ben-Younis, A.; Ujma, J.; Britt, H.; Cragolini, T.; Kalfas, S.; Cooper-Shepherd, D.; Tomczyk, N.; Giles, K.; Morris, M.; Akter, R.; Raleigh, D.; Thalassinou, K. Cyclic Ion Mobility-Collision Activation Experiments Elucidate Protein Behavior in the Gas Phase. *J. Am. Soc. Mass Spectrom.* **2021**, *32*, 1545–1552.
- (9) Weis, P. Structure Determination of Gaseous Metal and Semi-Metal Cluster Ions by Ion Mobility Spectrometry. *Int. J. Mass Spectrom.* **2005**, *245*, 1–13.
- (10) Bocker, E. R.; Anderson, S. E.; Northrop, B. H.; Stang, P. J.; Bowers, M. T. Structures of Metallosupramolecular Coordination Assemblies Can Be Obtained by Ion Mobility Spectrometry-Mass Spectrometry. *J. Am. Chem. Soc.* **2010**, *132*, 13486–13494.

- (11) Chan, Y. T.; Li, X.; Yu, J.; Carri, G. A.; Moorefield, C. N.; Newkome, G. R.; Wesdemiotis, C. Design, Synthesis, and Traveling Wave Ion Mobility Mass Spectrometry Characterization of Iron(II)- and Ruthenium(II)-Terpyridine Metallomacrocycles. *J. Am. Chem. Soc.* **2011**, *133*, 11967–11976.
- (12) Lloyd Williams, O. H.; Rijs, N. J. Reaction Monitoring and Structural Characterisation of Coordination Driven Self-Assembled Systems by Ion. *Front. Chem.* **2021**, *9*, No. 682743.
- (13) Geue, N.; Winpenny, R. E. P.; Barran, P. E. Structural Characterisation Methods for Supramolecular Chemistry That Go beyond Crystallography. *Chem. Soc. Rev.* **2022**, *51*, 8–27.
- (14) Ujma, J.; Benoit, F.; Barran, P. E. Analysis of Metallosupramolecular Assemblies Using Advanced Mass Spectrometry Techniques. In *Comprehensive Supramolecular Chemistry*, Vol 6; 2017; pp 389–403.
- (15) Wang, H.; Guo, C.; Li, X. Multidimensional Mass Spectrometry Assisted Metallo-Supramolecular Chemistry. *CCS Chem.* **2022**, *4*, 785–808.
- (16) Li, X.; Chan, Y. T.; Newkome, G. R.; Wesdemiotis, C. Gradient Tandem Mass Spectrometry Interfaced with Ion Mobility Separation for the Characterization of Supramolecular Architectures. *Anal. Chem.* **2011**, *83*, 1284–1290.
- (17) Mallis, C. S.; Saha, M. L.; Stang, P. J.; Russell, D. H. Topological Characterization of Coordination-Driven Self-Assembly Complexes: Applications of Ion Mobility-Mass Spectrometry. *J. Am. Soc. Mass Spectrom.* **2019**, *30*, 1654–1662.
- (18) Baksi, A.; Schneider, E. K.; Weis, P.; Krishnadas, K. R.; Ghosh, D.; Hahn, H.; Pradeep, T.; Kappes, M. M. Nanogymnastics: Visualization of Intercluster Reactions by High-Resolution Trapped Ion Mobility Mass Spectrometry. *J. Phys. Chem. C* **2019**, *123*, 28477–28485.
- (19) Troiani, F.; Ghirri, A.; Affronte, M.; Carretta, S.; Santini, P.; Amoretti, G.; Piligkos, S.; Timco, G.; Winpenny, R. E. P. Molecular Engineering of Antiferromagnetic Rings for Quantum Computation. *Phys. Rev. Lett.* **2005**, *94*, 1–4.
- (20) Timco, G. A.; Carretta, S.; Troiani, F.; Tuna, F.; Pritchard, R. J.; Muryn, C. A.; McInnes, E. J. L.; Ghirri, A.; Candini, A.; Santini, P.; Amoretti, G.; Affronte, M.; Winpenny, R. E. P. Engineering the Coupling between Molecular Spin Qubits by Coordination Chemistry. *Nat. Nanotechnol.* **2009**, *4*, 173–178.
- (21) Lockyer, S. J.; Chiesa, A.; Brookfield, A.; Timco, G. A.; Whitehead, G. F. S.; McInnes, E. J. L.; Carretta, S.; Winpenny, R. E. P. Five-Spin Supramolecule for Simulating Quantum Decoherence of Bell States. *J. Am. Chem. Soc.* **2022**, *144*, 16086–16092.
- (22) Li, X. Z.; Tian, C. B.; Sun, Q. F. Coordination-Directed Self-Assembly of Functional Polynuclear Lanthanide Supramolecular Architectures. *Chem. Rev.* **2022**, *122*, 6374–6458.
- (23) Wang, H.; Li, Y.; Li, N.; Filosa, A.; Li, X. Increasing the Size and Complexity of Discrete 2D Metallosupramolecules. *Nat. Rev. Mater.* **2021**, *6* (2), 145–167.
- (24) McTernan, C. T.; Davies, J. A.; Nitschke, J. R. Beyond Platonic: How to Build Metal-Organic Polyhedra Capable of Binding Low-Symmetry, Information-Rich Molecular Cargoes. *Chem. Rev.* **2022**, *122* (11), 10393–10437.
- (25) Saha, R.; Mondal, B.; Mukherjee, P. S. Molecular Cavity for Catalysis and Formation of Metal Nanoparticles for Use in Catalysis. *Chem. Rev.* **2022**, *122* (14), 12244–12307.
- (26) McInnes, E. J. L.; Timco, G. A.; Whitehead, G. F. S.; Winpenny, R. E. P. Heterometallic Rings: Their Physics and Use as Supramolecular Building Blocks. *Angew. Chem., Int. Ed.* **2015**, *54*, 14244–14269.
- (27) Shrivastav, V.; Nahin, M.; Hogan, C. J.; Larriba-Andaluz, C. Benchmark Comparison for a Multi-Processing Ion Mobility Calculator in the Free Molecular Regime. *J. Am. Soc. Mass Spectrom.* **2017**, *28*, 1540–1551.
- (28) Geue, N.; Bennett, T. S.; Ramakers, L. A. I.; Timco, G. A.; Armentrout, P. B.; McInnes, E. J. L.; Burton, N. A.; Winpenny, R. E. P.; Barran, P. E. Adduct Ions as Diagnostic Probes for Metallosupramolecular Complexes Using Ion Mobility Mass Spectrometry. *ChemRxiv*; 17th October 2022, DOI: 10.26434/chemrxiv-2022-lmq8t.
- (29) Ballesteros, B.; Faust, T. B.; Lee, C. F.; Leigh, D. A.; Muryn, C. A.; Pritchard, R. G.; Schultz, D.; Teat, S. J.; Timco, G. A.; Winpenny, R. E. P. Synthesis, Structure, and Dynamic Properties of Hybrid Organic-Inorganic Rotaxanes. *J. Am. Chem. Soc.* **2010**, *132*, 15435–15444.
- (30) Larsen, F. K.; Overgaard, J.; Christensen, M.; McIntyre, G. J.; Timco, G.; Winpenny, R. E. P. Metal Distribution and Disorder in the Crystal Structure of $[\text{NH}_2\text{Et}_2][\text{Cr}_7\text{MF}_8(\text{tBuCO}_2)_{16}]$ Wheel Molecules for M = Mn, Fe, Co, Ni, Cu, Zn and Cd. *Acta Crystallogr.* **2014**, *B70*, 932–941.
- (31) Baker, M. L.; Piligkos, S.; Bianchi, A.; Carretta, S.; Collison, D.; McDouall, J. J. W.; McInnes, E. J. L.; Mutka, H.; Timco, G. A.; Tuna, F.; Vadivelu, P.; Weihe, H.; Güdel, H. U.; Winpenny, R. E. P. Modification of the Magnetic Properties of a Heterometallic Wheel by Inclusion of a Jahn-Teller Distorted Cu(II) Ion. *Dalton Trans.* **2011**, *40*, 8533–8539.
- (32) Nose, H.; Chen, Y.; Rodgers, M. T. Energy-Resolved Collision-Induced Dissociation Studies of 1,10-Phenanthroline Complexes of the Late First-Row Divalent Transition Metal Cations: Determination of the Third Sequential Binding Energies. *J. Phys. Chem. A* **2013**, *117*, 4316–4330.
- (33) Nose, H.; Rodgers, M. T. Energy-Resolved Collision-Induced Dissociation Studies of 2,2'-Bipyridine Complexes of the Late First-Row Divalent Transition-Metal Cations: Determination of the Third-Sequential Binding Energies. *Chempluschem* **2013**, *78*, 1109–1123.
- (34) Engelhardt, L. P.; Muryn, C. A.; Pritchard, R. G.; Timco, G. A.; Tuna, F.; Winpenny, R. E. P. Octa-, Deca-, Trideca-, and Tetradecanuclear Heterometallic Cyclic Chromium-Copper Cages. *Angew. Chem., Int. Ed.* **2008**, *47*, 924–927.
- (35) Wang, L.; Song, B.; Khalife, S.; Li, Y.; Ming, L. J.; Bai, S.; Xu, Y.; Yu, H.; Wang, M.; Wang, H.; Li, X. Introducing Seven Transition Metal Ions into Terpyridine-Based Supramolecules: Self-Assembly and Dynamic Ligand Exchange Study. *J. Am. Chem. Soc.* **2020**, *142*, 1811–1821.
- (36) Boiadjev, S. E.; Lightner, D. A. Steric Size in Conformational Analysis. Steric Compression Analyzed by Circular Dichroism Spectroscopy. *J. Am. Chem. Soc.* **2000**, *122*, 11328–11339.
- (37) Jackson, V. E.; Felmy, A. R.; Dixon, D. A. Prediction of the pKa's of Aqueous Metal Ion +2 Complexes. *J. Phys. Chem. A* **2015**, *119*, 2926–2939.
- (38) Hoshino, N.; Nakano, M.; Nojiri, H.; Wernsdorfer, W.; Oshio, H. Templating Odd Numbered Magnetic Rings: Oxovanadium Heptagons Sandwiched by β -Cyclodextrins. *J. Am. Chem. Soc.* **2009**, *131*, 15100–15101.
- (39) Ochsenbein, S. T.; Tuna, F.; Rancan, M.; Davies, R. S. G.; Muryn, C. A.; Waldmann, O.; Bircher, R.; Sieber, A.; Carver, G.; Mutka, H.; Fernandez-Alonso, F.; Podlesnyak, A.; Engelhardt, L. P.; Timco, G. A.; Güdel, H. U.; Winpenny, R. E. P. Studies of Finite Molecular Chains: Synthesis, Structural, Magnetic and Inelastic Neutron Scattering Studies of Hexa- And Heptanuclear Chromium Horseshoes. *Chem. - A Eur. J.* **2008**, *14*, 5144–5158.
- (40) Hall, Z.; Politis, A.; Robinson, C. V. Structural Modeling of Heteromeric Protein Complexes from Disassembly Pathways and Ion Mobility-Mass Spectrometry. *Structure* **2012**, *20*, 1596–1609.
- (41) Beveridge, R.; Migas, L. G.; Payne, K. A. P.; Scrutton, N. S.; Leys, D.; Barran, P. E. Mass Spectrometry Locates Local and Allosteric Conformational Changes That Occur on Cofactor Binding. *Nat. Commun.* **2016**, *7*, 1–9.
- (42) Zhou, M.; Wysocki, V. H. Surface Induced Dissociation: Dissecting Noncovalent Protein Complexes in the Gas Phase. *Acc. Chem. Res.* **2014**, *47*, 1010–1018.
- (43) Vallejo, D. D.; Rojas Ramírez, C.; Parson, K. F.; Han, Y.; Gadkari, V. V.; Ruotolo, B. T. Mass Spectrometry Methods for Measuring Protein Stability. *Chem. Rev.* **2022**, *122*, 7690.
- (44) Figgis, B. N.; Hitchman, M. A. *Ligand Field Theory and Its Applications*; Wiley-VCH: New York, Chichester, 2000.

(45) Larsen, F. K.; McInnes, E. J. L.; El Mkami, H.; Overgaard, J.; Piligkos, S.; Rajaraman, G.; Rentschler, E.; Smith, G. A.; Smith, G. M.; Boote, V.; Jennings, M.; Timco, G. A.; Winpenny, R. E. P. Synthesis and Characterization of Heterometallic $\{Cr_7M\}$ Wheels. *Angew. Chem., Int. Ed.* **2003**, *42*, 101–105.

(46) Fort, K. L.; Van De Waterbeemd, M.; Boll, D.; Reinhardt-Szyba, M.; Belov, M. E.; Sasaki, E.; Zschoche, R.; Hilvert, D.; Makarov, A. A.; Heck, A. J. R. Expanding the Structural Analysis Capabilities on an Orbitrap-Based Mass Spectrometer for Large Macromolecular Complexes. *Analyst* **2018**, *143*, 100–105.

(47) Giles, K.; Ujma, J.; Wildgoose, J.; Pringle, S.; Richardson, K.; Langridge, D.; Green, M. A Cyclic Ion Mobility-Mass Spectrometry System. *Anal. Chem.* **2019**, *91*, 8564–8573.

(48) Shvartsburg, A. A.; Smith, R. D. Fundamentals of Traveling Wave Ion Mobility Spectrometry. *Anal. Chem.* **2008**, *80*, 9689–9699.

(49) Morsa, D.; Gabelica, V.; De Pauw, E. Effective Temperature of Ions in Traveling Wave Ion Mobility Spectrometry. *Anal. Chem.* **2011**, *83*, 5775–5782.

(50) Merenbloom, S. I.; Flick, T. G.; Williams, E. R. How Hot Are Your Ions in TWAVE Ion Mobility Spectrometry? *J. Am. Soc. Mass Spectrom.* **2012**, *23*, 553–562.

(51) Ervin, K. M.; Armentrout, P. B. Translational Energy Dependence of $Ar^+ + XY \rightarrow ArX^+ + Y$ ($XY = H_2, D_2, HD$) from Thermal to 30 eV c.m. *J. Chem. Phys.* **1985**, *83*, 166–189.

(52) Chakraborty, P.; Baksi, A.; Khatun, E.; Nag, A.; Ghosh, A.; Pradeep, T. Dissociation of Gas Phase Ions of Atomically Precise Silver Clusters Reflects Their Solution Phase Stability. *J. Phys. Chem. C* **2017**, *121*, 10971–10981.

(53) Ruotolo, B. T.; Benesch, J. L. P.; Sandercock, A. M.; Hyung, S. J.; Robinson, C. V. Ion Mobility-Mass Spectrometry Analysis of Large Protein Complexes. *Nat. Protoc.* **2008**, *3*, 1139–1152.

(54) Stow, S. M.; Causon, T. J.; Zheng, X.; Kurulugama, R. T.; Mairinger, T.; May, J. C.; Rennie, E. E.; Baker, E. S.; Smith, R. D.; McLean, J. A.; Hann, S.; Fjeldsted, J. C. An Interlaboratory Evaluation of Drift Tube Ion Mobility-Mass Spectrometry Collision Cross Section Measurements. *Anal. Chem.* **2017**, *89*, 9048–9055.

(55) Frisch, M. J.; Trucks, G. W.; Schlegel, H. B.; Scuseria, G. E.; Robb, M. A.; Cheeseman, J. R.; Scalmani, G.; Barone, V.; Petersson, G. A.; Nakatsuji, H.; Li, X.; Caricato, M.; Marenich, A. V.; Bloino, J.; Janesko, B. G.; Gomperts, R.; Mennucci, B.; Hratchian, H. P.; Ortiz, J. V.; Izmaylov, A. F.; Sonnenberg, J. L.; Williams-Young, D.; Ding, F.; Lipparini, F.; Egidi, F.; Goings, J.; Peng, B.; Petrone, A.; Henderson, T.; Ranasinghe, D.; Zakrzewski, V. G.; Gao, J.; Rega, N.; Zheng, G.; Liang, W.; Hada, M.; Ehara, M.; Toyota, K.; Fukuda, R.; Hasegawa, J.; Ishida, M.; Nakajima, T.; Honda, Y.; Kitao, O.; Nakai, H.; Vreven, T.; Throssell, K.; Montgomery, J. A. J.; Peralta, J. E.; Ogliaro, F.; Bearpark, M. J.; Heyd, J. J.; Brothers, E. N.; Kudin, K. N.; Staroverov, V. N.; Keith, T. A.; Kobayashi, R.; Normand, J.; Raghavachari, K.; Rendell, A. P.; Burant, J. C.; Iyengar, S. S.; Tomasi, J.; Cossi, M.; Millam, J. M.; Klene, M.; Adamo, C.; Cammi, R.; Ochterski, J. W.; Martin, R. L.; Morokuma, K.; Farkas, O.; Foresman, J. B.; Fox, D. *J. Gaussian 16*; Revision C.01. Gaussian, Inc.: Wallingford CT2016.

(56) Grimme, S.; Antony, J.; Ehrlich, S.; Krieg, H. A Consistent and Accurate Ab Initio Parametrization of Density Functional Dispersion Correction (DFT-D) for the 94 Elements H-Pu. *J. Chem. Phys.* **2010**, *132*, 154104.

(57) Hay, P. J.; Wadt, W. R. Ab Initio Effective Core Potentials for Molecular Calculations. Potentials for K to Au Including the Outermost Core Orbitals. *J. Chem. Phys.* **1985**, *82*, 299–310.

(58) *CrysAlisPro Software System Version 1.171.37.33*. Rigaku Corporation: Oxford, UK, 2018.

(59) Sheldrick, G. M. A Short History of SHELX. *Acta Crystallogr* **2008**, *A64*, 112–122.

(60) Dolomanov, O. V.; Bourhis, L. J.; Gildea, R. J.; Howard, J. A.; Puschmann, H. OLEX2: A Complete Structure Solution, Refinement and Analysis Program. *J. Appl. Crystallogr.* **2009**, *42*, 339–341.